Sustainable Energy & Fuels

ROYAL SOCIETY OF CHEMISTRY

PAPER

View Article Online
View Journal

Cite this: DOI: 10.1039/d6se00180g

Real-time monitoring of dynamic changes in Li-metal deposition and dissolution using a MHz impedance sensor

Keisuke Ishikawa, * Shogo Komagata, * Hiroki Kondo and Masanori Ishigaki

Li-metal deposition represents a critical degradation pathway in Li-ion batteries, rendering real-time monitoring of this process essential for ensuring safe operation. In this study, Li-metal deposition and dissolution are monitored using a sensor that measures the real part of the impedance (Re(Z)) in the MHz range. The MHz-range Re(Z) is highly sensitive to Li-metal, enabling compact sensor implementation and rendering it well-suited for monitoring applications. Thus, a highly accurate sensor is developed to monitor Li-metal deposition and dissolution dynamics. For proof of principle, an *operando* cross-sectional observation cell with sensor monitoring is employed to validate the ability to capture Li-metal dynamics. It is also confirmed that this approach is effective for application in commercial 18 650 cells, and cycle testing demonstrates that deposition and dissolution evolve with degradation. This work provides a robust tool for investigating Li-metal dynamics and offers a pathway for real-time monitoring of safer and more reliable battery systems.

Received 13th February 2026
Accepted 29th April 2026

DOI: 10.1039/d6se00180g

rsc.li/sustainable-energy

Introduction

Li-ion batteries (LIBs) are widely used in many applications. However, multiple degradation mechanisms limit the lifetimes and safety of LIBs,[1,2] and accurate identification of the battery state is essential for efficient operation.[3] One critical degradation mechanism is Li-metal deposition.[1,2,4,5] The deposited Li-metal can become electrically isolated, redissolve as Li^+, re-intercalate, or form a solid electrolyte interphase (SEI).[6,7] In this study, Li remaining in metallic form is defined as residual Li-metal, irrespective of its electrical connectivity, whereas Li that was once deposited but is no longer present in metallic form is regarded as having undergone dissolution, which includes redissolution as Li^+, re-intercalation into graphite, and consumption through SEI formation. Li-metal can also trigger internal short circuits and lower the thermal stability.[8,9] In practice, charge/discharge operation is restricted to a pre-characterised non-deposition window with safety margins. Although real-time detection of Li-metal deposition could enable closed-loop suppression, this approach still allows transient deposition; therefore, safety can only be ensured if dissolution is also monitored. Incorporating real-time monitoring of both Li-metal deposition and dissolution into control strategies would therefore enable relaxation of overly restrictive charging limits, allowing the full capability of the battery to be utilised safely and efficiently.

Several non-destructive techniques, including electrochemical impedance spectroscopy (EIS), have been proposed to detect Li-metal deposition.[10–17] However, these methods generally fail to capture Li-metal dissolution and EIS presents challenges for real-time measurement. To observe Li-metal deposition and dissolution, the anode response must be isolated from the overlapping time constants of the cathode and the SEI, while also being separated from other degradation modes. This requires dense frequency sampling, which conflicts with the sparse sampling principle of dynamic EIS.[18] Observing the dynamics of Li-metal using EIS therefore remains challenging.

Previously, our group reported that the real part of the impedance (Re(Z)) in the MHz range decreases when Li-metal deposition occurs.[19] In principle, this enables the observation of both Li-metal deposition and dissolution. The MHz-range Re(Z) has been shown to correlate with the thermal runaway onset temperature, which decreases with increasing Li-metal deposition, and therefore can be used to estimate the approximate extent of Li-metal deposition.[9] The MHz-regime response is governed by electronic properties and geometry rather than by ionic transport, thereby avoiding the time-constant separation issues exhibited by conventional EIS.[20] Owing to the eddy currents that are induced by electromagnetic effects,[21] high-frequency currents concentrate on the anode surface where the Li-metal is deposited.[22] The resulting contrast in conductivity between the deposited Li-metal and the carbon matrix redirects the current pathways, thereby altering the eddy current losses. Consequently, the MHz-range Re(Z) monotonically decreases with the amount of deposited Li-metal.[19]

Secondary Batteries Research-Domain, Toyota Central R&D Labs., Inc., Nagakute, Aichi 4801192, Japan. E-mail: k-ishikawa@mosk.tytlabs.co.jp; komagata@mosk.tytlabs.co.jp

One benefit of MHz-range Re(Z) measurement is the ease of miniaturising the sensor. MHz-range Re(Z) can be measured using two methods, a vector network analyser (VNA)-based method and a sensor based on LCR series resonance.[19] Using a VNA, high-precision measurements were achieved in the MHz range, with a coefficient of variation of <0.2%.[23] In the sensor concept, Re(Z) is calculated from the attenuation of the damped oscillation generated by the LCR resonance.[19,24,25] With VNA-level accuracy, the sensor has the potential to monitor Li-metal dynamics. Accordingly, to enable reliable safety quantification across varying environments, the sensor must exhibit high linearity, low temperature-dependent error, and minimal battery voltage-induced error. To meet these requirements, we propose a new post-processing circuit and algorithm, which reduce the battery voltage-induced error to less than ±0.05%. It is therefore considered that this highly accurate sensor would be capable of monitoring Li-metal dynamics.

With the above considerations in mind, the aim of the current study is to demonstrate that the proposed sensor can detect both Li-metal deposition and dissolution. For proof of principle, a cross-sectional observation cell is used to visualise Li-metal dynamics while acquiring sensor measurements and supporting the validity of the principle. Additionally, commercial 18 650 cells are tested using various charge/discharge protocols and during cycling. The variation in the MHz-range Re(Z) with the amounts of Li-metal deposition is evaluated as a function of the C-rate. Cycling tests are also performed to demonstrate the ability of MHz-range Re(Z) to capture degradation state-dependent changes in Li-metal deposition and dissolution. Ultimately, this work aims to demonstrate the feasibility of monitoring under practical operating conditions, while providing guidelines for developing control strategies that maximise battery performance.

Results and discussion

Principle of the proposed MHz impedance sensor

Fig. 1a presents a schematic overview of the proposed sensor for detecting Li-metal deposition. The sensor induces a damped oscillating resonant current in the battery to calculate MHz-range Re(Z) from the resulting damping factor. MHz-range Re(Z) is sensitive to Li-metal deposition, where the MHz-range Re(Z) decreases during Li-metal deposition and recovers upon dissolution. Therefore, the residual drop in MHz-range Re(Z) can be used to identify residual Li-metal deposition. To implement this method, an LC resonator and a peak-hold (PH) circuit were integrated, with a microcontroller controlling the operation timing of the LC resonator and PH circuit and performing MHz-range Re(Z) calculations.

Fig. 1b shows a photographic image of the sensor circuit attached to a battery, while Fig. 1c shows the detailed circuit diagram. Based on this diagram, the operating principle of the sensor is explained as follows. Here, an inductor L_r, capacitor C_r, and switch SW_r are connected to the battery in series. Additionally, R_b is the real part of the impedance of the battery. Upon closing SW_r, the LCR network carries a damped resonance whose damping factor α is governed by R_b at the resonant angular frequency $\omega_0 = \sqrt{1/L_rC_r - \alpha^2}$, and the transformer (M = mutual inductance) produces the voltage output $V_p(t)$, as expressed using the following equation:

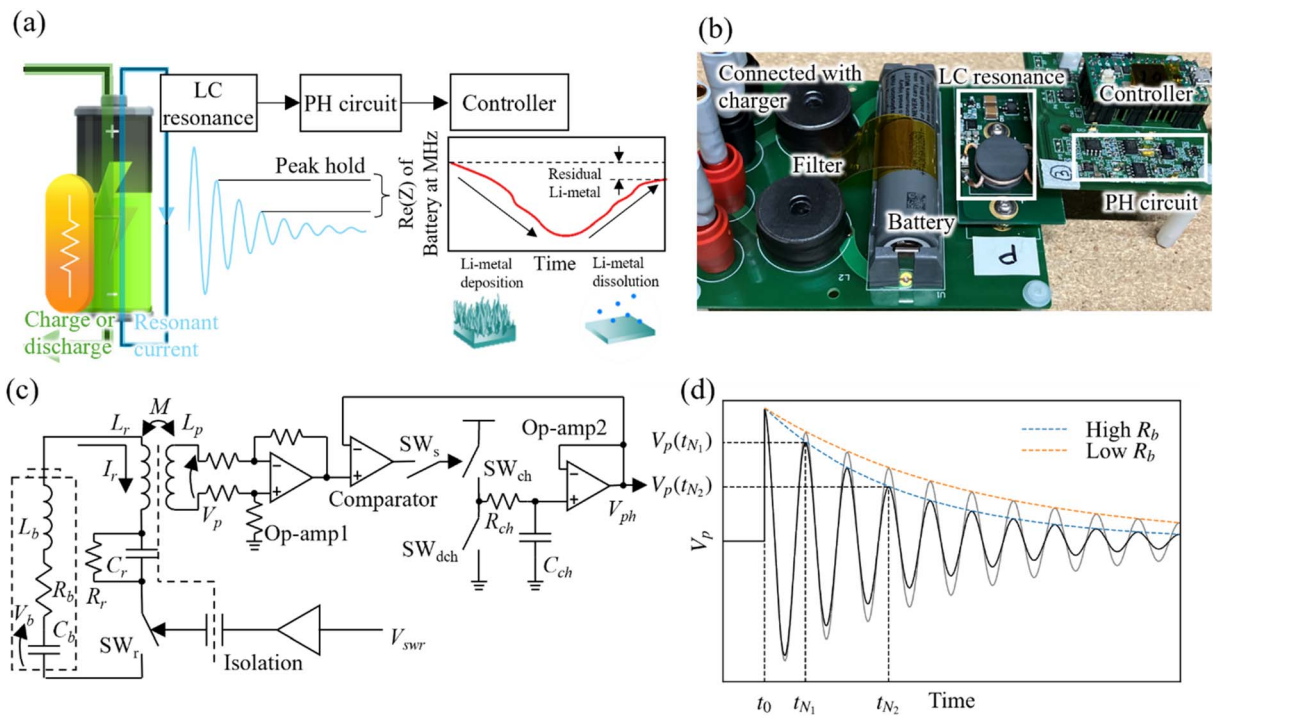

Fig. 1 (a) Schematic overview of the proposed sensor for detecting Li-metal deposition. (b) Photographic image of the sensor circuit attached to a battery. (c) Detailed sensor circuit diagram. (d) Damped oscillation waveform produced by the sensor and the resulting attenuation factor as a function of the battery resistance.

$$V_p(t) = \frac{M V_b \sqrt{\alpha^2 + \omega_0^2}}{L_r \omega_0} e^{-\alpha t} \sin(\omega_0 t - \beta), \quad (1)$$

where β is the phase angle and V_b is the battery voltage. As shown in Fig. 1c, a smaller value of R_b results in a slower damping of V_p. Since the damping factor is given by $\alpha(=R_b/2L_r)$, R_b can be obtained by determining α from eqn (1). However, the amplitude of the V_p waveform varies depending on the battery voltage V_b. Therefore, measuring the damping factor from the V_p waveform requires accurate measurement of the battery voltage along with high-speed sampling to capture signals in the MHz range, which renders the accurate measurement of R_b difficult. Thus, the proposed method removes unknown parameters (including V_b), and R_b is obtained from the following expression:

$$R_b = \frac{2L_r}{t_{N_2} - t_{N_1}} \ln\left|\frac{V_p(t_{N_1})}{V_p(t_{N_2})}\right|, \quad (2)$$

where t_{N_1} and t_{N_2} satisfy $t_{N_1} < t_{N_2}$ and

$$\sin(\omega_0 t_{N_1} - \beta) = \sin(\omega_0 t_{N_2} - \beta). \quad (3)$$

By applying eqn (2), R_b can be determined without dependence on the cell voltage (state of charge, SOC). The procedures employed to optimise the two peak positions and select the sensor parameters are described in the SI.

To capture these two peaks, a PH circuit was employed, as shown in Fig. 1a. Notably, conventional PH circuits struggle to acquire MHz waveforms without overshoot/undershoot, in the case of damped oscillations. The proposed PH circuit uses a pulse-selection switch to capture the desired peak. With repeated excitations, the held value converges to that peak, enabling high-accuracy measurement to be performed, as shown in Fig. S1 and S2. It was verified that the circuit can hold the peak voltage and that measurement is feasible at sampling rates of a few kHz.

Sensor measurement accuracy

The accuracy of the prototype sensor was evaluated using the parameters and components listed in Table S1. A chip resistor of a known value was connected in series with a direct current (DC) biased capacitor to emulate a battery. Fig. 2a shows the measurement accuracy when the chip resistance is varied from 100 to 1000 mΩ. Notably, a measurement error of less than ±0.5 mΩ (±0.2%) was achieved.

The voltage-dependent error was evaluated by varying the voltage of the DC biased capacitor (simulating the battery voltage) from 2.8 to 4.2 V. For comparison, evaluations were performed using the VNA shunt-through method (which offers the highest measurement accuracy), the conventional sensor,[19] and the proposed sensor. As shown in Fig. 2b, the conventional sensor exhibited an error of ±0.29%, whereas the proposed sensor achieved an error of less than ±0.05%, which is comparable to that of the VNA-based method.

Furthermore, the temperature-dependent error was compared between the conventional and proposed sensors by varying the temperature from 0 to 60 °C at 3.5 V. As shown in Fig. 2c, the conventional sensor showed an error of ±0.61%, while the proposed sensor achieved an error of less than ±0.08%. These results demonstrate that the proposed sensor enables highly accurate R_b measurements to be performed across a wide range of battery voltages, temperatures, and resistances.

Cross-sectional observation cell

Subsequently, the ability of the proposed sensor to monitor Li-metal deposition and dissolution was verified using a cross-sectional observation cell. Fig. 3a shows a photographic image of the cross-sectional observation cell and the sensor. Additionally, Fig. 3b presents the corresponding charge/discharge profiles of the sensor, wherein R_b was measured at 1 MHz. As indicated by the error bars, changes in Li-metal dissolution lie within the error of the conventional method but are clearly observed as a meaningful change using the proposed sensor. Fig. 3c presents the cross-sectional images recorded at each stage of charge/discharge. In Fig. 3b and c, stages [1]–[5] represent the charging period, while stages [6]–[10] represent the discharging period. A movie presenting the correlation between the cross-sectional observations of the cell, the cell voltage, and R_b is available in the SI.

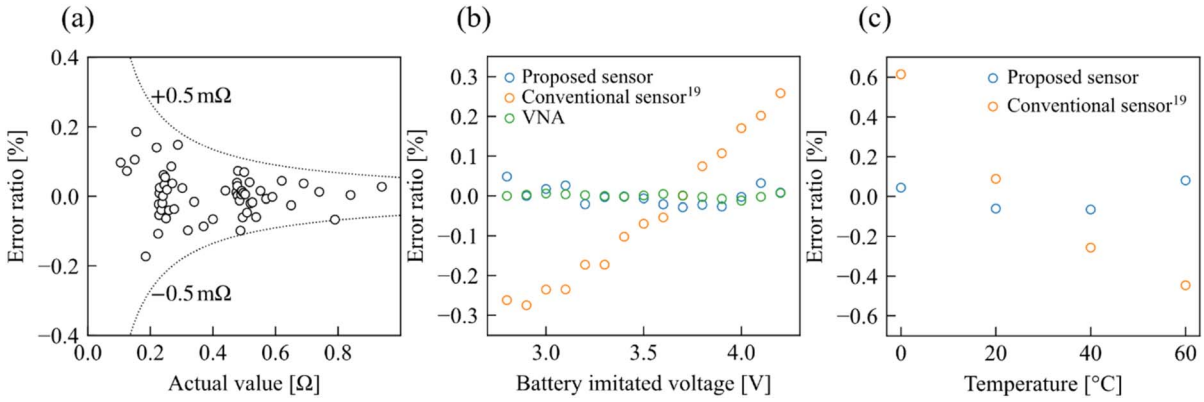

Fig. 2 (a) Linearity of the sensor when measuring chip resistors between 100 and 1000 mΩ. (b and c) Effect of the voltage and temperature on the sensor error ratio. The sensor characteristics were evaluated using a simulated battery where $C_b = 100$ μF and $R_b = 470$ mΩ.

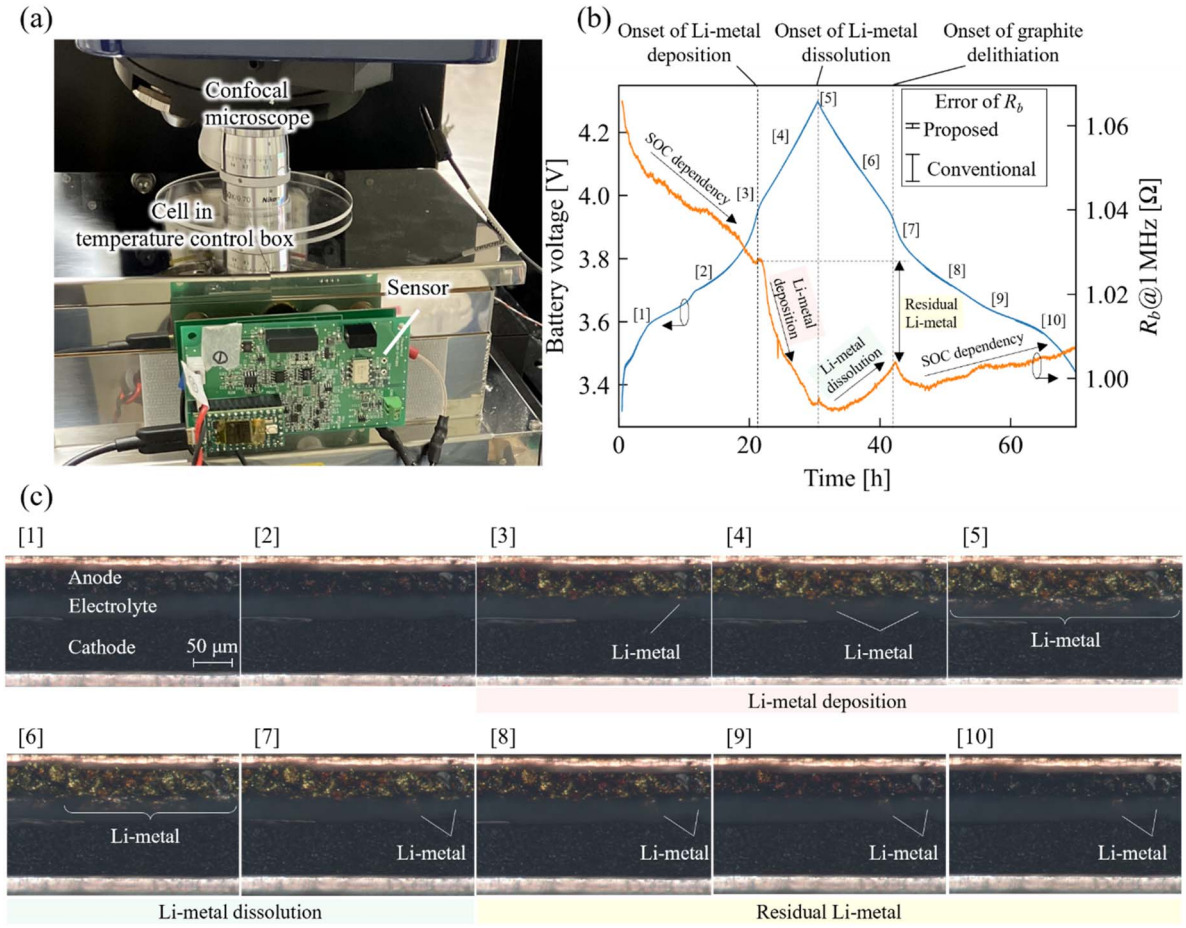

Fig. 3 (a) Photographic image of the cross-validation setup, showing the cross-sectional observation cell equipped with the sensor circuit. (b) Battery voltage and sensor output, R_b, recorded during an overcharge-induced Li-deposition/dissolution test. Error bars represent the voltage-dependent error derived from Fig. 2b. (c) Cross-sectional images of the cell acquired during the test shown in (b).

To pinpoint the onset of Li-metal deposition, an anode-limited design was employed in which the cathode capacity exceeded the anode capacity (N/P = 0.7). In this configuration, the anode becomes fully charged at a cell voltage of ~3.9 V, at which point Li-metal deposition begins. During the charging period at voltages <3.9 V, the colour of the graphite anode changed from black to blue, red, and gold, as shown in Fig. 3c (stages [1]–[3]), corresponding to the staged intercalation of Li-ions.[26,27] As shown in Fig. 3c (stages [3] and [4]), a voltage step near 3.9 V during charging marks the onset of Li-metal deposition. Also, the movie (SI) clearly shows the onset and subsequent growth of metallic lithium deposition during charging at voltages above ~3.9 V. On the other hand, as indicated in Fig. 3c (stages [6] and [7]), delithiation from graphite resumes near 3.9 V during discharge.

A change in the slope of R_b was observed at the 3.9 V boundary. The change in the slope of R_b below 3.9 V was inferred to stem from conductivity changes in the graphite anode because the conductivity of graphite increases with lithiation (*i.e.*, at higher SOC). Measurement of the in-plane Re(Z) of graphite at 1 MHz confirmed that Re(Z) decreases with increasing SOC, as shown in Fig. S7. Conversely, above 3.9 V, the graphite is fully lithiated and its conductivity stabilises. The obtained results therefore indicate that the sensor detects R_b changes caused by Li-metal deposition across the 3.9 V threshold.

In the charging region above 3.9 V, R_b decreases as Li-metal deposition increases, as shown in Fig. 3c (stages [3]–[5]), whereas during discharge, R_b increases with Li-metal dissolution, as shown in Fig. 3c (stages [5]–[7]). This behaviour indicates that R_b varies with the amount of Li-metal present. Meanwhile, even when the battery voltage reaches 3.9 V during discharging, R_b remains lower than that observed at the same voltage during charging. As confirmed by the images shown in Fig. 3c (stages [7]–[10]), these results indicate that residual Li-metal is present.

To confirm that the observed change in R_b is associated with residual Li-metal, the results of charge/discharge without overcharge are shown in Fig. S9. Although the same type of cell was used as that in the cross-sectional observation experiments, the offset resistance was smaller because the sensor was connected directly to the cell without the terminal used in the cross-sectional observation setup. Since the magnitude of R_b change is comparable, the range of the right y-axis was set to be the

same as that in Fig. 3b. Charging was limited to 3.8 V to avoid Li-metal deposition. An SOC-dependent change in R_b similar to that in Fig. 3b was observed. Under the conditions without Li-metal deposition, R_b returned to its original value after charge/discharge. This result suggests that the decrease in R_b remaining after discharge in Fig. 3b is attributable to residual Li-metal.

The relationship between the Li-metal images at the anode cross-section and the sensor-measured value of R_b at 1 MHz confirms that the proposed sensor can identify Li-metal deposition and dissolution, along with residual Li-metal. These Li-metal dynamics were previously undetectable using conventional sensors, as the signals were obscured by measurement error. These observations therefore demonstrate that the high accuracy of the proposed sensor is essential for distinguishing these Li-metal dynamics.

Application to commercial 18 650 cells and challenges

Li-metal dynamics were further evaluated under various test conditions in commercial cells to demonstrate the practicality of the developed sensor. Commercial LIBs come in several package formats, including cylindrical, pouch, and prismatic cells. In this study, the evaluation was conducted using standardized cylindrical 18 650 cells. As 18 650 cells are standardized and widely utilized, they provide the most practical format for demonstrating broad applicability. While the results from the cross-sectional cell confirm that the sensor is applicable to pouch cells, demonstrating universal applicability across all such formats remains challenging due to the wide variety of sizes, terminal positions, and structures inherent in pouch and prismatic cells. Further validation using a broader range of pouch and prismatic cell configurations remains an important subject for future work.

Initially, to confirm the sensitivity of Re(Z) to Li-metal deposition in 18 650 cells and to identify the frequency of Re(Z) that exhibits the highest sensitivity, Fig. 4a shows the Re(Z) measured using a VNA before and after Li-metal deposition over 90 cycles of 2C charging. A greater reduction in Re(Z) was observed in the MHz range with increasing cycle numbers, reflecting ongoing Li-metal deposition. Based on the optimal peak sensitivity observed at 1 MHz, the sensor was configured to operate at this frequency.

Although the sensor measurement is thermally stable, the battery impedance varies with temperature. Fig. 4b shows the VNA-evaluated variation of Re(Z) in the MHz range at temperatures of 15, 25, and 30 °C, relative to 20 °C. In this frequency range, Re(Z) is strongly influenced by the electrode conductivity and therefore increases with temperature. A temperature difference of 5 °C resulted in an approximately 4% change in Re(Z). Given the substantial temperature rise during fast charging, the thermal contribution to Re(Z) is non-negligible compared with the signal changes induced by Li-metal deposition. Assessing this temperature dependence requires estimation of the internal temperature. Therefore, in this study, the analysis was limited to Re(Z) data obtained after a sufficient rest period following charge/discharge, when the battery temperature had stabilised at 20 °C, and the effects of temperature fluctuations during charge/discharge were not examined.

The SOC dependence of R_b was also evaluated in an 18 650 cell. Fig. 4c presents the results of Re(Z) measurements performed at 1 MHz as a function of the SOC, obtained using both the proposed sensor and a VNA. The VNA measurements were carried out at 20% SOC intervals, while the sensor performed continuous measurements during charging at 0.01C. These results confirm that the sensor is unaffected by the battery voltage variations associated with the SOC and that it achieves measurement accuracy comparable to that of the VNA. Furthermore, the 18 650 cell exhibits characteristics distinct from those of the pouch cell used in the cross-sectional observations. Unlike in the cross-sectional observation cell, the cylindrical cell is influenced by winding inductance and tab placement, and R_b can either increase or decrease.[19,28] A precise analysis of the SOC dependency therefore requires electromagnetic, electrochemical, and structural evaluations. In this study, the R_b values obtained at different SOCs were calibrated using Fig. 4c as a SOC-R_b map referenced to SOC = 0%. The low voltage-dependent error of the proposed sensor enables comparisons across different battery voltages (*i.e.*, SOCs), provided the calibration is valid. In future work, implementing dynamic SOC and temperature compensation should enable monitoring of more dynamic Li-metal behaviour during charge/discharge.

To confirm the measurement reproducibility of the sensor for 18 650 cells, the variation in the measured value was evaluated for repeated attachment/detachment of the cell 10 times and for five repeated charge/discharge cycles in which the cell was charged at 0.4C to 50% SOC and discharged at 0.1C to 0% SOC. The results of the cycling test are shown in Fig. S11. The standard deviation for the attachment/detachment test was 1.24 mΩ (0.23%), while the standard deviation at the same SOC during the five cycling tests was 0.5 mΩ (0.08%) or less. These values are much smaller than the battery's temperature and SOC dependence, demonstrating high measurement reproducibility of the proposed sensor.

The impact of Li-metal deposition on battery safety and degradation depends on the location and morphology of the deposited Li. The proposed sensor acquires only the real part of the impedance at a single frequency. Therefore, although it can be used to estimate the approximate extent of Li-metal deposition, it is difficult to identify its location and morphology. Information on the location and morphology of Li-metal deposition would be helpful for operating lithium-ion batteries more efficiently. On the other hand, from the viewpoint of safe operation, estimating the extent of Li-metal deposition using the proposed sensor is still sufficiently useful.

Various C-rate charging conditions in commercial 18 650 cells

We demonstrate that precise SOC and temperature calibrations are not strictly necessary for the practical application of the proposed sensor. Even with the current level of development, the sensor shows strong potential as a safety-diagnostic tool capable of detecting Li-metal behaviour in commercial batteries.

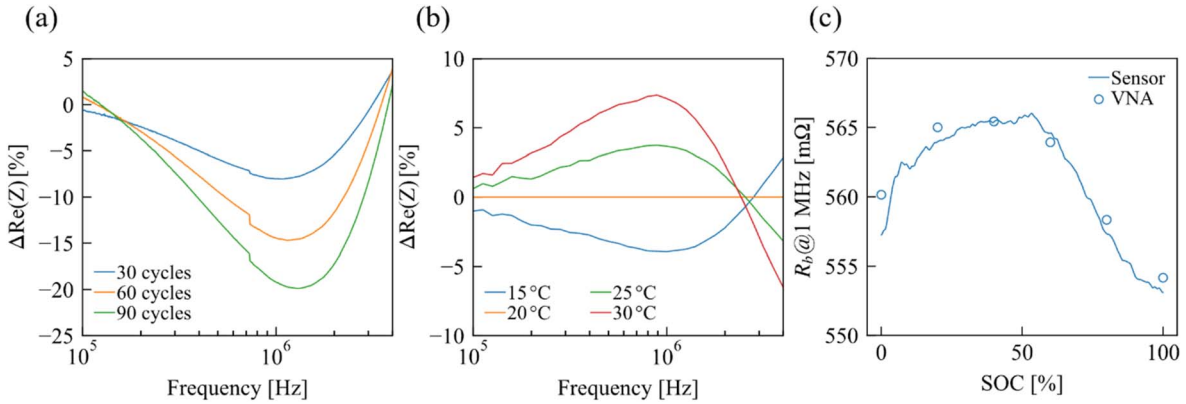

Fig. 4 (a) Change in R_b for an 18 650 cell relative to the initial value after 30, 60, and 90 cycles of 2C charge-cycling. (b) Temperature dependence of the MHz-range R_b value for the 18 650 cell. (c) SOC dependence of R_b at approximately 1 MHz for the 18 650 cell, as measured using the sensor and a VNA.

Using 18 650 cells, charging was performed at various C-rates, and Li-metal deposition and dissolution were evaluated based on the sensor-measured R_b. For this purpose, the tested cell was charged from 0 to 60% SOC (ΔSOC 60%) while increasing the charge rate by 0.2C each cycle (0.2–2.0C). After charging, a 1 h rest period was applied. Subsequently, the cells were discharged to 2.85 V at 0.2C, followed by a constant voltage discharge at 2.85 V for 3 h. Fig. 5a shows the recorded battery voltage V_b, battery-surface temperature T_b, sensor-measured R_b, and SOC-corrected R_b during the cycling test. The corresponding data for charging from 0 to 70% SOC (ΔSOC 70%) were evaluated, indicating that with repeated charging at higher C-rates, R_b decreases relative to its initial value across all SOC states, suggesting the presence of Li-metal deposition.

To evaluate the Li-metal dynamics more rigorously, the change in R_b was analysed at points A (1 h post-charge) and B (end of discharge), as shown in Fig. 5a. These points were selected to ensure identical SOC and temperature conditions. Fig. 5b and c show changes in R_b at points A and B, respectively, wherein the error bars represent the voltage-dependent error derived from Fig. 2b. At point A, a higher C-rate and a higher charging SOC consistently correlate with a decrease in R_b. This suggests that a higher C-rate and greater charging capacity lead to a greater amount of Li-metal deposition. In contrast, at Point B, no significant change is observed up to 1C. The R_b value, which decreased at Point A, recovers to its original level, suggesting Li-metal dissolution. As indicated by the error bars, the ability to evaluate not only Li-metal deposition but also dissolution is made possible solely by the enhanced precision of the proposed sensor.

To quantify this Li-metal dissolution, the change in R_b from point A to B was calculated, as shown in Fig. 5d. Specifically, the increase in R_b from point A to B indicates that a greater extent of Li-metal deposition leads to enhanced dissolution. If this Li-metal dissolution is insufficient, it is observed as residual Li-metal, as shown in Fig. 5c. A portion of this Li-metal becomes electrically isolated from the anode and persists within the battery as dead Li. The test results indicate that during charging at 1C or higher, the rate of Li-metal deposition exceeds that of dissolution, thereby compromising safety.

To evaluate the change in R_b produced by a single cycle at each C-rate, independent of the effects of residual Li-metal, the difference in R_b was calculated between point A and previous point B, as shown in Fig. 5e. A significant decrease in R_b was observed beyond 1C. On the other hand, Fig. 5d shows no abrupt change near 1C. These results further suggest that charging rates greater than 1C result in significant Li-metal deposition, thereby increasing the likelihood of Li-metal remaining as residue. To ensure safety, it is necessary to either ensure sufficient time for Li-metal dissolution or to charge at a C-rate that minimises deposition. The proposed sensor provides the critical metrics required to determine these optimal operating conditions.

Cycle degradation in commercial 18 650 cells

In the previous section, the characteristics of fresh cells were evaluated. However, in LIBs, the conditions for Li-metal deposition change due to degradation.[29,30] Since degradation states vary widely and are difficult to predict in advance, real-time evaluation is essential. It was therefore verified whether the proposed sensor can assess Li-metal deposition even at varying degradation states. To quantify the degradation-dependent changes in Li-metal deposition and dissolution and to show that these processes can be measured using the proposed sensor, 25 charge/discharge cycles were performed. These charge/discharge cycles were repeated using a fixed charging C-rate, following the conditions outlined in Fig. 5a.

Fig. 6a shows the cycle-by-cycle changes in R_b at points A (1 h post-charge) and B (end of discharge) during cycling at 1.6C with ΔSOC 60%. The observed change from point B to A (after the subsequent charge) suggests Li-metal deposition, while the change from point A to B suggests Li-metal dissolution. Here, dissolution refers to all processes by which deposited Li-metal no longer remains as metallic Li, including redissolution into the electrolyte, re-intercalation into the graphite anode, and consumption through a reaction with the electrolyte to form the SEI. The difference between deposition and dissolution

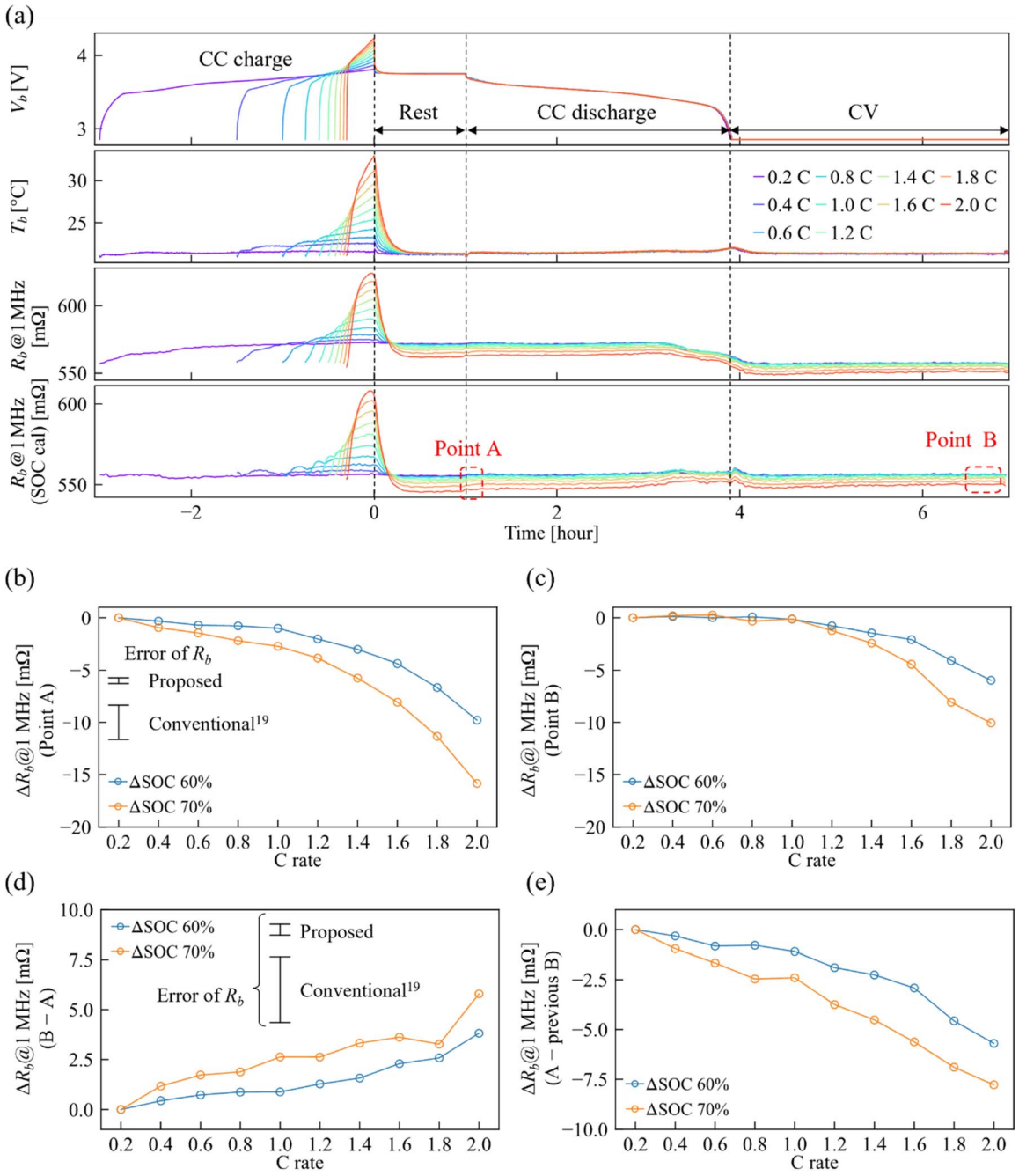

Fig. 5 (a) Stepwise C-rate test in which the charge rate was raised by 0.2C each cycle and charging was performed from 0 to 60% SOC. (b) Change in R_b at point A. (c) Change in R_b at point B. (d) Change in R_b evaluated from point A to point B. (e) Change in R_b evaluated from point B (immediately before charging) to point A. The error bars in panels (b) and (d) represent the voltage-dependent error derived from Fig. 2b.

corresponds to the amount of residual Li-metal. Upon increasing the number of cycles, both the deposition and dissolution amplitudes increased and the net R_b value drifted downward. These results suggest that with continued cycling, the extent of Li-metal deposition increases as the cell degrades, while also indicating that dissolution is incomplete during the discharge step, resulting in residual Li-metal build-up.

Fig. 6b shows the changes in R_b at point B for C-rates of 0.4, 1.0, and 1.6C, wherein charging was performed at ΔSOC 60% or 70%. The test performed at ΔSOC 70% at 1.6C was finalised upon reaching the upper-voltage limit after 23 cycles. In contrast, at 0.4C, the small amount of deposited Li-metal appeared to dissolve almost completely, and R_b remained nearly constant over approximately 10 cycles. Beyond this point, R_b began to decline and ultimately dropped by approximately 3 mΩ. This result is consistent with the finding that repeated rapid charging of LIBs causes heterogeneous degradation, and once this degradation exceeds a threshold, the battery becomes prone to rapid degradation accompanied by Li-metal

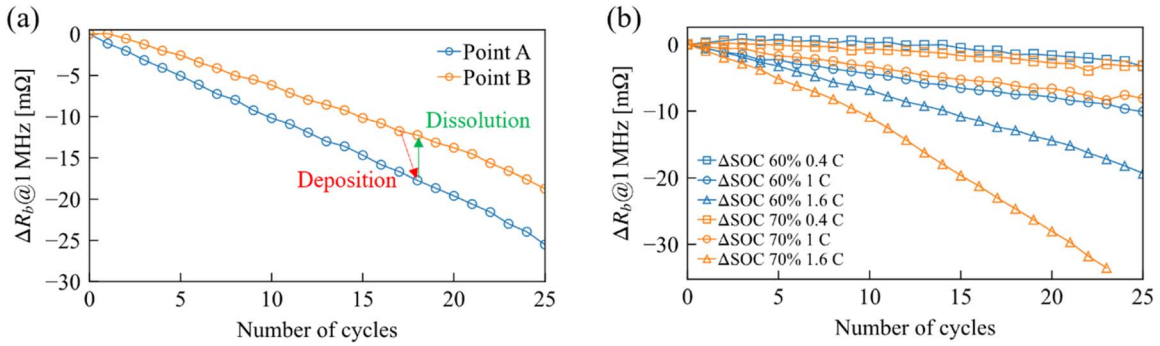

Fig. 6 (a) Changes in R_b at points A and B over 25 cycles at a charge rate of 1.6C. During each cycle, charging was performed under ΔSOC 60% conditions. (b) Changes in R_b at point B over 25 cycles at charge rates of 0.4, 1.0, and 1.6C (ΔSOC = 60% or 70%).

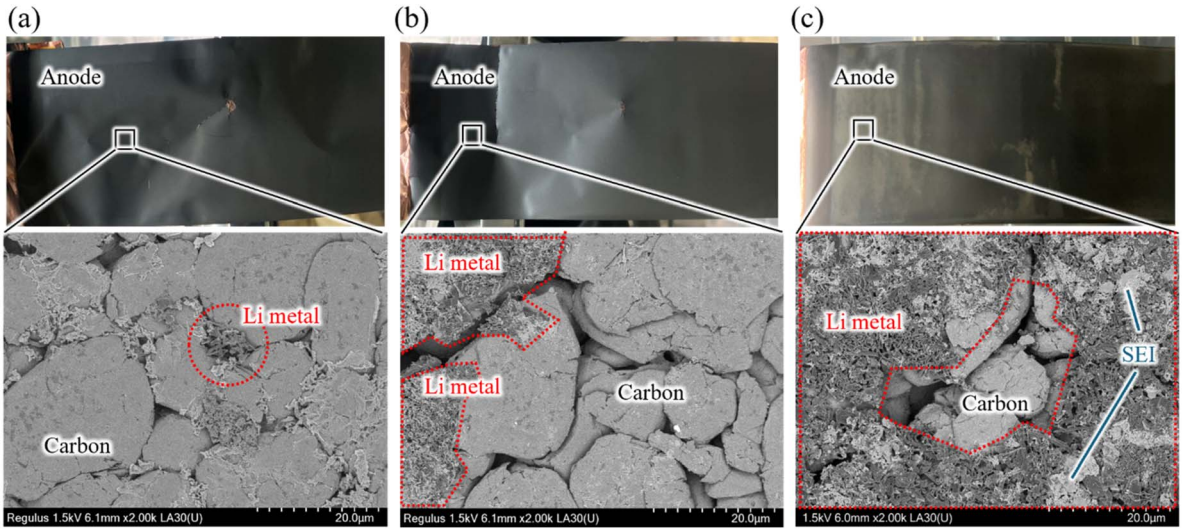

Fig. 7 Photographic images and SEM back-scattered electron images recorded for the disassembled anode after 25 cycles: (a) ΔSOC 60%, 0.4C; (b) ΔSOC 60%, 1C; and (c) ΔSOC 70%, 1.6C.

deposition.[31] Given the unpredictability of these degradation states, continuous monitoring using the sensor is essential.

Confirmation of Li-metal deposition *via* disassembly

After cycling, the three representative cells (0.4C, ΔSOC 60%; 1.0C, ΔSOC 60%; and 1.6C, ΔSOC 70%) were opened, and their anodes were examined by scanning electron microscopy (SEM) in the back-scattered electron mode as shown in Fig. 7, wherein the residues darker than the carbon matrix correspond to Li-metal. From Fig. 7a, it is evident that only a few isolated microscale Li-metal deposits are visible, consistent with the modest 3 mΩ decrease in R_b. Fig. 7b and c reveal progressively larger deposits, and in Fig. 7c, the Li-metal is clearly visible. These observations confirm that the proposed sensor can be used to quantify the amount of Li-metal deposition.

Conclusions

In summary, the real-time monitoring of Li-metal deposition and dissolution in LIBs was achieved using the developed sensor that measures MHz-range Re(Z) values. The proposed sensor implemented a new equation for R_b that is independent of V_b, along with a novel post-processing circuit. Importantly, these features resulted in accurate monitoring under varying V_b conditions. Using a cross-sectional observation cell, it was verified that the sensor tracks Li-metal dynamics, in addition to the resulting residual Li-metal fraction. In commercial 18 650 cells, the sensor resolved changes in R_b that were consistent with the amounts of deposition and dissolution. Cycling tests showed that these behaviours evolved with degradation and were observable in real-time. These results indicate that the proposed sensor can provide a basis for control strategies that retain safety, while maximising battery performance.

However, several challenges remain, including an improved feasibility for higher-capacity or parallel-connected cells and temperature compensation. Since higher-capacity cells exhibit smaller MHz-range Re(Z) values, greater accuracy is required. Additionally, an appropriate temperature calibration method for correcting the MHz-range Re(Z) values is needed. For practical long-term battery monitoring, another important challenge is to retain high measurement accuracy over extended operating periods while minimising the influence of

temperature drift, circuit drift, and external noise. Resolving these challenges will broaden the applicability of the sensor across various battery capacities and applications to enable safer, more efficient charge/discharge control.

Experimental section

Sensor operating conditions

Table S1 lists the sensor components and parameters required to calculate Re(Z) using eqn S9. These values were used for both the cross-sectional observation cell and the 18 650 cell evaluations. The power consumption of the sensor originates from a resistor R_r placed parallel to a capacitor C_r in the LCR resonator. When switch SW_r is ON, a battery voltage V_b is applied across R_r, causing current to flow and a capacitor C_r to be charged. After the switch turns OFF, the charge stored in C_r is discharged through R_r. The current through R_r during the ON period dominates the power consumption, whereas the contribution from charging and discharging C_r is negligible in comparison. To measure the single-peak value, the switch was switched ON/OFF 250 times. This process was repeated six times and the six resulting peak measurements were averaged to reduce noise. Considering that two peaks were measured per cycle, a total of $6 \times 250 \times 2 = 3000$ ON events existed per measurement. The energy consumed per measurement depends on V_b and is equal to $150\ V_b^2 \times 10^{-6}$ Wh. Because of the large capacity of the 18 650 cell, measurements were performed every 2 s. In contrast, measurements were performed every 15 s for the smaller cross-sectional cell. Fig. S10 shows the cumulative charge drawn by the sensor during charging, thereby accounting for its power consumption.

Evaluation of the SOC dependence of the high-frequency impedance

In-plane resistance measurements were conducted for the anode using the cell configurations shown in Fig. S4 and S5. The anode employed graphite (OMAC 1.5 S) as the active material, which had a composition of graphite/CMC/SBR = 98 : 1 : 1 (wt%). The slurry was coated on one side of a PET film to give a loading of 3.9 mg cm^{-2} and pressed to reach an active material density of 1.3 g cm^{-3}. Copper foil with ultrasonically welded Ni tabs was sealed at both ends of the electrode to enable current collection and was mechanically compressed using a custom jig, as described in Fig. S5. To minimize the influence of the current collector on the high-frequency impedance measurements, ~50 μm Kapton tape was applied over the collector areas. The cathode employed NCM(111) as the active material, which had a composition of NCM(111)/acetylene black/PVDF = 92 : 5 : 3 (wt%). The cathode was coated on one side of Al foil to give an NCM loading of 7 mg cm^{-2} and pressed to achieve an active material density of 2.5 g cm^{-3}.

The cells were fabricated by assembling the coated sides of the electrodes on either side of a separator and sealing them in an aluminum laminate pouch. The electrolyte (1 M $LiPF_6$ in EC/DMC/EMC = 3 : 4 : 3 vol.) was injected into the cell in an Ar-filled glove box. A uniform pressure of 1 kg cm^{-2} was applied using a spring-loaded jig and a 2 mm thick silicone rubber sheet.

Subsequently, a single constant-current (CC) conditioning cycle was applied at 0.1C (3.0–4.1 V, 20 °C), followed by charging to 4.1 V at 0.1C and aging at 60 °C for 6 h. After cooling to 20 °C, the cell was discharged to 3.0 V using the CC-CV (constant voltage) mode at 0.1C to prepare the test cell.

The test cell was adjusted to specific SOC in 20% increments of 0.1C. After each step, the cells were rested for 1 h to allow voltage relaxation. Subsequently, each cell was connected to a vector network analyzer (E5061B, Keysight) and stabilized for 1 h prior to performing the impedance measurements between 100 kHz and 100 MHz using the shunt-through method.[23]

Fig. S6 depicts the SOC dependence of Re(Z) at 1 MHz, wherein a decreasing trend in Re(Z) is observed with an increasing SOC. This trend is consistent with the previously reported relationship between the lithium content and the electronic conductivity in lithium-intercalated graphite compounds (LIGCs), as described by Basu *et al.*[32] Thus, the SOC dependence observed in the standard charge region was attributed to the variation in the electronic conductivity of the LIGC, which was associated with the extent of lithium intercalation into graphite.

Cross-sectional observations

Using the cell configurations shown in Fig. S7 and S8, cross-sectional observations were conducted in parallel with charge/discharge cycling and impedance measurements. The cathode consisted of NCM(111) as the active material, which had a composition of NCM(111)/acetylene black/PVDF = 92 : 5 : 3 (wt%). The slurry was coated on one side of Al foil to give a loading of 14 mg cm^{-2} and pressed to achieve an active material density of 2.5 g cm^{-3}. A commercially available single-side coated graphite anode (1.5 mAh cm^{-2}) was also employed. The cell was designed with an excess cathode capacity (N/P ratio ≈ 0.7), allowing lithium plating to occur even at low charge rates.

To minimize the influence of the current collector in uncoated regions during the high-frequency impedance measurements, ~50 μm Kapton tape was applied to the bare mask areas. Cross-sectional imaging was then performed using confocal laser scanning microscopy (Lasertec ECCS B320).

The cell was assembled by placing the electrodes face-to-face through a separator and sealing them in an aluminum laminate pouch. A 1 mm-thick EPDM sheet and a clamping jig were used to apply a uniform pressure of 8.5 kg cm^{-2}. The cross-section for observation was prepared using a cutter that was incorporated within the confocal system. The electrolyte (1 M $LiPF_6$ in EC/DMC/EMC = 3 : 4 : 3 vol.) was injected into the cell in an Ar-filled glove box, and the pouch was sealed immediately.

A single conditioning charge cycle was applied at 0.2C (3.0–3.9 V, 20 °C), followed by charging to 3.9 V at 0.2C and aging at 60 °C for 6 h. After subsequent cooling to 20 °C, the cell was discharged to 3.0 V using a CC–CV protocol at 0.2C to prepare the test cell.

Cross-sectional observations were performed at 20 °C using a thermostatic system. During cycling (Solartron 1287), the impedance at 1 MHz was measured using an impedance sensor

and the confocal microscopy images were captured simultaneously.

Test conditions for the commercial 18 650 cells

All tests performed on the commercial 18 650 cells were conducted in a temperature-controlled chamber maintained at 20 °C. All tests began and ended with a capacity check. Specifically, the capacity checks consisted of CC charging at 0.1C (0.1C = 0.26 A) to 4.2 V, CV charging at 4.2 V for 3 h, a 10 min rest, CC discharging at 0.1C to 2.85 V, and CV discharging at 2.85 V for 3 h. For the experiments shown in Fig. 5, each cycle was performed as follows. After the capacity check, the cell was charged at 0.2C under CC conditions to either from 0 to 60% SOC (ΔSOC 60%) or 70% SOC (ΔSOC 70%), rested for 1 h, discharged under CC conditions at 0.2C to 2.85 V, and then discharged under CV conditions at 2.85 V for 3 h. The CC charge rate was increased by 0.2C in each subsequent cycle until reaching 2.0C. No cycle reached the 4.2 V cutoff under these conditions. In the experiments shown in Fig. 6, six charge protocols (ΔSOC 60% or 70% at 0.4, 1.0, or 1.6C) were tested. All discharge steps were performed under CC conditions at 0.2C to 2.85 V followed by CV conditions at 2.85 V for 3 h. These tests were conducted over 25 cycles, except for the ΔSOC 70% and 1.6C condition, which was terminated after 23 cycles upon reaching the 4.2 V cutoff.

Author contributions

Keisuke Ishikawa designed and developed the sensor circuit; planned, executed, and analysed the experiments, including those performed using cylindrical cells; and wrote the manuscript. Shogo Komagata characterised the cross-sectional observation cell, planned, executed, and analysed the combined sensor experiments, performed SEM observation of the disassembled cells, and contributed to writing of the manuscript. Hiroki Kondo supervised the experiments. Masanori Ishigaki co-designed and developed the sensor circuit and supervised the experiments. All authors discussed the results and revised the manuscript accordingly.

Conflicts of interest

There are no conflicts to declare.

Data availability

All data needed to evaluate the conclusions in the paper are provided in the paper and the supplementary information (SI). Supplementary information: methods and real-time monitoring video of the cross-sectional observation cell. See DOI: https://doi.org/10.1039/d6se00180g.

Acknowledgements

The authors would like to thank Dr Tsuyoshi Sasaki and Dr Yoshinari Makimura for their valuable advice and insightful discussions.

References

1 D. H. Jeon, S. Kim and R. Hempelmann, *J. Power Sources*, 2025, **646**, 237242.
2 Y. Wang, H. Xiang, Y. Y. Soo and X. Fan, *Renewable Sustainable Energy Rev.*, 2025, **207**, 114915.
3 R. Li, L. Bao, L. Chen, C. Zha, J. Dong, N. Qi, R. Tang, Y. Lu, M. Wang, R. Huang, K. Yan, Y. Su and F. Wu, *Sci. Bull.*, 2023, **68**, 3055–3079.
4 J. He, J. Meng and Y. Huang, *J. Power Sources*, 2023, **570**, 232965.
5 X. Lin, K. Khosravinia, X. Hu, J. Li and W. Lu, *Prog. Energy Combust. Sci.*, 2021, **87**, 100953.
6 Z. M. Konz, B. M. Wirtz, A. Verma, T. Y. Huang, H. K. Bergstrom, M. J. Crafton, D. E. Brown, E. J. McShane, A. M. Colclasure and B. D. McCloskey, *Nat. Energy*, 2023, **8**, 450–461.
7 Y. Che, X. Hu, X. Lin, J. Guo and R. Teodorescu, *Energy Environ. Sci.*, 2023, **16**, 338–371.
8 Y. Li, X. Feng, D. Ren, M. Ouyang, L. Lu and X. Han, *ACS Appl. Mater. Interfaces*, 2019, **11**, 46839–46850.
9 K. Ishikawa, S. Komagata, R. Morimoto, M. Ishigaki, H. Kondo and T. Sasaki, *ECS Trans.*, 2024, **113**, 9.
10 W. Mei, Y. Zhang, Y. Li, P. Zhuo, Y. Chu, Y. Chen, L. Jiang, H. Zhou, J. Sun and Q. Wang, *Energy Storage Mater.*, 2024, **66**, 103193.
11 I. D. Campbell, M. Marzook, M. Marinescu and G. J. Offer, *J. Electrochem. Soc.*, 2019, **166**, A725–A739.
12 W. Yu, Z. Xing, W. Ruixi, Z. Tao, X. Peitao, S. Yupeng, X. Yukang and L. Yajie, *Energy Storage Mater.*, 2024, **69**, 103369.
13 L. Spitthoff, P. J. S. Vie, M. S. Wahl, J. Wind and O. S. Burheim, *J. Electroanal. Chem.*, 2023, **944**, 117627.
14 J. C. Burns, D. A. Stevens and J. R. Dahn, *J. Electrochem. Soc.*, 2015, **162**, A959–A964.
15 T. Sun, Z. Li, G. Zhu, L. Wang, D. Ren, T. Shen, L. Lu, Y. Zheng, X. Han and M. Ouyang, *Electrochim. Acta*, 2024, **496**, 144512.
16 M. Koseoglou, E. Tsioumas, D. Ferentinou, N. Jabbour, D. Papagiannis and C. Mademlis, *J. Power Sources*, 2021, **512**, 230508.
17 S. Drvarič Talian, G. Kapun, J. Moškon, R. Dominko and M. Gaberšček, *Nat. Commun.*, 2025, **16**, 2030.
18 X. Zhang, Y. Lu, J. Shi, Y. Liu, H. Cheng and Y. Lu, *EcoMat*, 2025, **7**, e70018.
19 M. Ishigaki, K. Ishikawa, T. Usuki, H. Kondo, S. Komagata and T. Sasaki, *Nat. Commun.*, 2023, **14**, 7275.
20 A. Ch. Lazanas and M. I. Prodromidis, *ACS Meas. Sci. Au*, 2023, **3**, 162–193.
21 E. E. Kriezis, H. D. Tsiboukis, S. M. Panas and J. A. Tegopoulos, *Proc. IEEE*, 1992, **80**, 1559–1589.
22 B. Li, Y. Chao, M. Li, Y. Xiao, R. Li, K. Yang, X. Cui, G. Xu, L. Li, C. Yang, Y. Yu, D. P. Wilkinson and J. Zhang, *Electrochem. Energy Rev.*, 2023, **6**, 1–46.
23 K. Ishikawa, T. Usuki, S. Komagata, R. Morimoto and M. Ishigaki, *IEEE Trans. Instrum. Meas.*, 2025, **74**, 1–12.

24 C. Li, J. Mao, Q. Wu, Y. Deng, J. Wu, W. Li and X. He, *Energies*, 2021, **14**, 7490.
25 D. Simatupang, A. Benshatti and S. Y. Park, *Batteries*, 2023, **9**, 104.
26 S. P. Rangarajan, C. Fear, T. Adhikary, Y. Barsukov, G. Dadheech and P. P. Mukherjee, *Cell Rep. Phys. Sci.*, 2023, **4**, 101740.
27 T. Gao, Y. Han, D. Fraggedakis, S. Das, T. Zhou, C. N. Yeh, S. Xu, W. C. Chueh, J. Li and M. Z. Bazant, *Joule*, 2021, **5**, 393–414.
28 T. F. Landinger, G. Schwarzberger and A. Jossen, *IEEE Trans. Electromagn. Compat.*, 2020, **62**, 1524–1533.
29 T. Bond, S. Gasilov, R. Dressler, R. Petibon, S. Hy and J. R. Dahn, *J. Electrochem. Soc.*, 2025, **172**, 030512.
30 N. Wassiliadis, J. Kriegler, K. A. Gamra and M. Lienkamp, *J. Power Sources*, 2023, **561**, 232586.
31 T. R. Tanim, P. P. Paul, V. Thampy, C. Cao, H. G. Steinrück, J. Nelson Weker, M. F. Toney, E. J. Dufek, M. C. Evans, A. N. Jansen, B. J. Polzin, A. R. Dunlop and S. E. Trask, *Cell Rep. Phys. Sci.*, 2020, **1**, 100114.
32 S. Basu, C. Zeller, P. J. Flanders, C. D. Fuerst, W. D. Johnson and J. E. Fischer, *Mater. Sci. Eng.*, 1979, **38**, 275–283.